Research Square

Preprints are preliminary reports that have not undergone peer review.
They should not be considered conclusive, used to inform clinical practice,
or referenced by the media as validated information.

Tumor intrinsic regulation of PD-L1 and of interferon Type I via an SLC25A1-driven mitochondrial pathway, influences the anti-tumor immune response

Maria Laura Avantaggiati

ma364@georgetown.edu

Georgetown University Medical Center https://orcid.org/0000-0001-8361-3440

Rami Mosaoa

Georgetown University Medical Center

Maha Moussa

Georgetown University Medical Center

Aditya Kavuturu

Georgetown University Medical Center

Salan Preet Kaur

Georgetown University Medical Center

Garrett Graham

Georgetown University Medical Center

Chis Albanese

Georgetown University Medical Center

Cecil Han

Georgetown University Medical Center

Marta Catalfamo

Georgetown University Medical Center

Article

Keywords:

Posted Date: November 13th, 2026

DOI: https://doi.org/10.21203/rs.3.rs-11500903/v1

License: This work is licensed under a Creative Commons Attribution 4.0 International License.
Read Full License

Additional Declarations: There is no conflict of interest

Tumor intrinsic regulation of PD-L1 and of interferon Type I *via* an SLC25A1-driven mitochondrial pathway, influences the anti-tumor immune response

Rami Mosaoa[1,2,#], Maha Moussa[2,3], Aditya Kavuturu[2], Salan Preet Kaur[2], Garrett Graham[2], Chris Albanese[2], Cecil Han[2], Marta Catalfamo[2,3], Maria Laura Avantaggiati[2,#]

[1] Department of Biochemistry, Faculty of Science, King Abdulaziz University, Jeddah, Saudi Arabia

[2] Georgetown University Medical Center, Lombardi Comprehensive Cancer Center, Washington, D.C., USA

[3] Georgetown University Medical Center, Department of Microbiology and Immunology, Washington, D.C., USA

Correspondence:

Maria Laura Avantaggiati: ma364@georgetown.edu

Rami Mosaoa: rmosaoa@kau.edu.sa

Abstract

Immune checkpoint blockade produces durable responses in some cancers, yet tumor-intrinsic regulators that influence therapeutic sensitivity remain incompletely understood. Here, we identify the mitochondrial citrate carrier SLC25A1 as a determinant of anti-PD-L1 antibody therapy responsiveness through a dual mechanism. SLC25A1 activates a mitochondrial-to-nuclear retrograde signaling by promoting cytosolic accumulation of mitochondrial DNA, which engages the cGAS–STAT1 pathway establishing a viral mimicry state that induces the IFN-I response. This response is particularly enriched in cancer stem cell populations, consistent with the established role of SLC25A1 in promoting tumor stemness and therapeutic resistance. Moreover, SLC25A1 controls PD-L1 protein abundance through a newly identified fumarate-Keap1 pathway, in which fumarate suppresses Keap1 leading to enhanced PD-L1 expression. In vivo, tumors with high SLC25A1 expression display enhanced sensitivity to PD-L1 blockade, associated with an IFN-I response and grow more rapidly in the absence of anti-PD-L1 treatment. These findings establish SLC25A1 as a novel regulator of mitochondria-driven IFN-I signaling and PD-L1 stability. They further suggest that SLC25A1 enables tumors to exploit PD-L1 for immune evasion while simultaneously creating an intrinsic vulnerability to checkpoint blockade. Thus, SLC25A1 may represent both a biomarker of therapeutic response and a target for improving immunotherapy efficacy.

INTRODUCTION

Immune checkpoint inhibitors (ICIs) have transformed therapeutic strategies for various malignancies, particularly lung cancer and melanoma [1-3]. Although durable and objective responses are observed in a subset of patients, a considerable number of patients do not respond to treatment, limiting the overall clinical benefit. Several factors influence the response to ICIs, including the tumor immunogenicity and the composition of the tumor immune microenvironment (TIME). Favorable responses are often associated with an inflamed TIME, characterized by infiltration of $CD8^+$ T cells, dendritic cells, and M1 macrophages, along with expression of Major Histocompatibility Complex (MHC) class I and II molecules. Conversely, "cold" tumors, which exhibit minimal immune cell infiltration and reduced antigenicity, are less responsive to ICIs [4-6]. Consequently, strategies aimed at converting cold tumors into inflamed tumors are a focus of ongoing investigations.

Given that tumor cells frequently up-regulate PD-L1 as a mechanism to evade immune surveillance, understanding the regulation of PD-L1 stability is also of significant interest. High PD-L1 expression often correlates with improved responses to ICIs, and inhibition of PD-L1 degradation pathways in certain tumor contexts has been proposed as a strategy to enhance immunotherapy efficacy. For instance, CDK4/6 inhibitors (e.g., palbociclib) have been shown to stabilize PD-L1 and to synergize with PD-L1 blockade [7-10]. Conversely, in tumors with sufficient immunogenicity, promoting PD-L1 degradation may facilitate the recruitment of effector immune cells and enhance tumor rejection [11]. Thus, elucidating the mechanisms regulating PD-L1 turnover has clinical relevance.

Recent evidence suggests that cancer cells can autonomously activate IFN-I pathways through a "virus mimicry" state, induced by the aberrant presence of endogenous nucleic acids in the cytosol [26,27]. A virus mimicry state can be therapeutically triggered by DNA demethylating agents, which reactivate normally silenced transposable elements, selectively affecting cancer stem cell populations [27,28]. Similarly, radiation therapy induces IFN-I responses through DNA damage-mediated cytosolic DNA accumulation, potentially enhancing the efficacy of immunotherapy [29]. Low levels of cytosolic DNA

appear to be a common feature in many cancers, leading to chronic, low-level IFN-I signaling [30]. Furthermore, the cytoplasmic presence of micronuclei resulting from chromosomal segregation errors can activate IFN-I pathways and has been associated with increased metastatic potential [31]. Collectively, these findings suggest that the context, the upstream triggering signals, as well as the magnitude and quality of IFN-I activation are critical determinants of its effects on tumor progression and therapeutic outcomes. However, it remains incompletely clear which tumor-intrinsic factors, independent of exogenous therapeutic interventions, are responsible for inducing virus mimicry states and regulate PD-L1 expression.

We have shown before that the main function of SLC25A1 consists of transporting citrate bi-directionally in and out of the mitochondria, while bringing malate inside [32-35]. Our previous mechanistic studies, which also involved the development of the most potent SLC25A1 inhibitor, CTPI-2, demonstrated that by regulating the flux of citrate/malate across the mitochondria, SLC25A1 promotes OXPHOS, maintains adequate TCA cycle flux, and allows metabolic adaptation promoting tumor progression [33,34]. We now show here that SLC25A1 regulates the response to anti-PD-L1 therapy and recruits IFN-I signaling. We also uncover a novel fumarate–Keap1–PD-L1 regulatory axis and propose that tumors with high levels of expression of SLC25A1 and IFN-I signaling have intrinsic vulnerability to checkpoint blockade.

Results

SLC25A1 elicits a mitochondrial-to-nucleus retrograde signaling that induces the antiviral IFN-I response.

We have shown before that SLC25A1 is frequently, but not universally expressed in several cancer cell lines and in metastatic lymph node biopsies derived from patients affected by Non-Small Cell Lung Cancer (NSCLC) [34]. To expand these observations, we interrogated a tumor array platform derived from NSCLC and patient-derived cancer cells [34]. As shown in Fig. 1A, the expression of SLC25A1 is variable in NSCLC, with some tumors showing elevated levels and others with intermediate or no expression. Similarly, SLC25A1 expression was elevated in some patient-derived tumors relative to normal adjacent tissues, but was completely absent in a subset of the patient-derived cells (e.g., T3, T6 and T7; Fig. 1 B).

These findings confirm the heterogeneous expression of SLC25A1 in NSCLC and identify tumors with high or low SLC25A1 expression, providing a rationale for investigating the biological consequences of its differential expression.

To identify the pathways that are directly under the control of SLC25A1, we initially employed H1299 lung cancer or B16F0 melanoma cell lines (both of which have very low SLC25A1 expression), which were stably transfected with a vector encoding for SLC25A1, resulting in moderately high expression of the protein (SLC25A1^{high}), Fig. 1C. To identify the transcriptional program driven by SLC25A1, we then performed transcriptomic profiling in SLC25A1^{low} or SLC25A1^{high} H1299 cells grown in spheroid conditions, to model the three-dimensional architecture of tumors. Notably, the results of the gene expression arrays revealed induction of many genes and signal pathways involved in the regulation of the anti-tumor immune response. These included a Foxp3 signature that controls the development and function of regulatory T (Treg) cells, Treg signal pathways and others (Fig. 1D). Among these signatures, the IFN-Iα and IFN-I response were very robustly induced and included a broad spectrum of Interferon-Stimulated Genes (ISGs), as well as the cytosolic DNA sensors GMP-AMP synthase, cGAS (Fig. 1E). The major histocompatibility complex class I (MHC-I) *HLA-A*, *HLA-B*, and *HLA-E* were also up-regulated, likely due to IFN-I activation and/or enhanced immunogenicity of SLC25A1-enriched spheroids.

We then validated the expression array data by assessing the mRNA levels of members of the ISG family with qRT-PCR. This approach confirmed the induction of a large gene set typical of the IFN-I

response in SLC25A1-expressing spheroids (Fig. 2A). To rule out that the induction of the IFN-I response is a cell type-specific phenomenon, we assessed the ISGs mRNA levels in murine melanoma B16F0 SLC25A1^{high} cells. Similar to H1299 cells, we observed induction of the ISGs by SLC25A1 in B16F0 as well (Fig. 2B). Similar results were also obtained in the kidney embryonic carcinoma 293T cell line (not shown). Importantly, the previously identified SLC25A1 inhibitor, CTPI-2, blunted the expression of ISGs in naïve H1299 spheres. In addition, Mouse Embryonic Fibroblasts (MEFs) lacking one *Slc25a1* allele (*Slc25a1+/-*) display reduced expression of ISGs relative to wild type MEFs (Supplementary Fig. 1 A,B). As expected, both cGAS and STAT1 protein levels were strongly induced by SLC25A1 (Fig. 2C).

Given recent evidence suggesting that activation of IFN-I signaling particularly in the cancer stem cell population (CSC), and our previous work demonstrating that SLC25A1 favors the expansion of the CSCs [17,34], we next explored whether SLC25A1 drives activation of the IFN-I pathway specifically within this population. Similar to embryonic and adult stem cells, CSCs from different cancer types can be identified and isolated based on the expression of stemness-associated surface markers, including CD133, CD44, and low CD24. To test the hypothesis that IFN-I activation is preferentially enriched within CSCs, SLC25A1^{high} spheroids were cultured for three days, followed by isolation of CSCs using fluorescence-activated cell sorting (FACS) based on surface expression of CD133, CD44, and CD24. The expression of interferon-stimulated genes (ISGs) in the isolated CSC population was subsequently analyzed by qRT-PCR. The results of these experiments demonstrated that IFNb1 and a subset of ISGs were more prominently expressed in the CD133-positive cell population compared to CD133-negative cells as well as in the CD44-positive/CD24-negative population (Fig. 2 D,E).

These findings reveal, for the first time, a physiological role for SLC25A1 in regulating IFN-I signaling in tumor CSCs. They further identify this protein as a mediator of mitochondria-to-nucleus retrograde signaling, an essential communication pathway through which mitochondria transmit signals to the nucleus to regulate the transcriptional program [36,37].

SLC25A1 promotes cytosolic mtDNA accumulation inducing a virus mimicry state and IFN-I activation.

The IFN-I response is activated under normal physiological conditions by the presence of exogenous (e.g., viral) or endogenous nucleic acids in the cytosol, which are in turn sensed by the Pattern Recognition Receptors (PRRs), including cGAS, which specifically recognizes cytosolic DNA [26,38,39]. This activation leads to a cascade of events involving the induction of Interferon Regulatory Factor 3 and 7 (IRF3/7), of interferon-induced protein with tetratricopeptide repeats 2 (IFIT2), which culminates in the induction of IFN-α and IFN-β. These cytokines initiate autocrine and paracrine signaling loops by binding to their receptors (IFNAR1/2) and activating the Janus Kinase/Signal Transducers and Activators of Transcription (JAK/STAT) pathway, ultimately resulting in the amplification of IFN-I signaling *via* STAT proteins. We therefore sought to investigate whether SLC25A1 induces this pathway by promoting mtDNA accumulation in the cytosol. To this end, we used primers designed to amplify regions of mitochondrial genes including *Cytochrome B (CYTB), NADH Dehydrogenase (ND2) and 16S ribosomal RNA gene (16S)*. The scheme of the mtDNA genes used in these experiments is shown in Supplementary Fig. 2A and the position of the primers employed is shown therein (closed balls). We found a significant increase in the levels of cytosolic mtDNA in both H1299 and 293T SLC25A1^{high} cells (Fig. 3A,B).

mtDNA can exit the mitochondria *via* the Mitochondria Permeability Transition Pore (MPTP). Therefore, we inhibited the opening of the MPTP with Cyclosporine A (CsA), which suppresses pore opening by binding to cyclophilin D. We observed a significant reduction in the ISGs expression levels in CsA treated spheres relative to untreated cells (Fig. 3C), indicating a role for MPTP opening in the induction of the IFN-I response. To further confirm the involvement of mtDNA, we next studied the effect of mtDNA depletion on the induction of the ISGs by employing well-established protocols where mtDNA depletion was achieved by chronically treating cells with a very low concentration of Ethidium Bromide (EtBr) [e.g., 40]. At low concentrations, EtBr intercalates into mtDNA preventing replication, while having no observable effect on genomic DNA. mtDNA depletion was validated by quantifying the ratio of mtDNA to nuclear genomic DNA in total cell extracts using q-PCR (Fig. 3D). First, the assessment of the levels of mtDNA in the cytosolic

fractions of EtBr-treated *versus* untreated cells demonstrated a marked decrease in cytosolic mtDNA accumulation in the treated cells, consistent with the observed total mtDNA depletion and as expected (Fig. 3E). Second, a clear reduction in ISG expression levels was observed in EtBr-treated cells, correlating with the depletion of total mtDNA and the diminished cytosolic accumulation of mtDNA (Fig. 3F).

To subsequently validate that the cGAS/STAT1 pathway is induced by SLC25A1 downstream of cytosolic mtDNA release, we conducted shRNA-mediated knockdown of either cGAS or STAT1 and subsequently evaluated the ISG mRNA levels. We found that the knockdown of either cGAS or STAT1 resulted in a marked reduction of ISG expression compared to cells transduced with control shRNA (Supplementary Fig. 2 B).

Together, these findings show that SLC25A1 promotes the release of mitochondrial DNA into the cytosol, triggering the cGAS-STAT1 pathway and establishing a virus-mimicry state that amplifies type I interferon signaling (Fig.3G).

SLC25A1 induces PD-L1 expression in cell intrinsic and cell extrinsic fashion. In tumor cells, PD-L1 expression can be induced and amplified through autocrine and paracrine signaling loops involving interferons, cytokines and growth factors released by tumor cells within the tumor microenvironment [41-43]. Given the newly identified role of SLC25A1 in mediating immuno-regulatory pathways and IFN-I activation, we sought to determine whether this protein also influences PD-L1 expression levels in an autocrine and/or paracrine manner (depicted in Fig. 4A). We found that PD-L1 protein was markedly up-regulated in SLC25A1^{high} H1299 (Fig. 4B). To rule out differences in the genetic background, we next assessed whether genetic or pharmacological inhibition of SLC25A1 influences PD-L1 expression in different cell lines. Treatment with the SLC25A1 inhibitor CTPI-2 significantly reduced PD-L1 protein levels, and the knockdown of SLC25A1 using a previously validated shRNA construct produced a similar decrease in the HCC827 lung cancer cell line, which naturally exhibits high endogenous PD-L1 expression (Fig. 4C,D). Furthermore, the inhibitory effect of CTPI-2 on PD-L1 expression was also evaluated in the

H1975 and HCC1937 cell lines, as well as in a patient-derived tumor cell line (T5) yielding similar results (Fig. 4E), supporting the conclusion that, in certain cell types, PD-L1 expression is regulated by SLC25A1 activity. Given the fundamental role played by cell extrinsic signals, in a complementary experimental setting, we examined the effects of the culture supernatants on recipient cells. We found that PD-L1 expression was increased in cells exposed to the supernatants derived from SLC25A1-expressing spheres (Fig. 4F).

The SLC25A1-mediated induction of PD-L1 is at least in part mediated by the ubiquitin adapter Keap1. Under normal physiological conditions, IFN-I up-regulates PD-L1 expression to promote immune homeostasis and prevent excessive inflammation and tissue damage. However, tumor cells exploit this pathway to promote immune evasion [41-43]. In keeping with the previous finding that SLC25A1 induces IFN-I signaling, we next explored whether the PD-L1 induction is dependent upon the IFN-I activation and the virus mimicry state triggered by SLC25A1. Contrary to this idea, mtDNA depletion led to PD-L1 upregulation, likely due to impaired mitochondrial respiration and increased lactic acid production [34], which is well known to increase PD-L1 levels (Fig. 5A) [44]. Similarly, the knock-down of the IFNAR1 receptor, cGAS or STAT1 only modestly reduced PD-L1 mRNA and protein levels in SLC25A1^{high} cells (Fig. 5B, C, D). Collectively, the data suggested the existence of additional molecular mechanisms by which SLC25A1 influences PD-L1 expression.

We and others have previously shown that SLC25A1 promotes the tricarboxylic (TCA) cycle, enhancing the availability of several TCA cycle intermediates, including citrate, fumarate, malate, and succinate, as well as of itaconate, an immunoregulatory TCA cycle metabolite derived from cis-aconitate. [34]. Given the emerging role of metabolic products and TCA cycle intermediates as immunoregulatory signaling metabolites capable of modulating inflammatory, hypoxic, and immune pathways linked to PD-L1 regulation, we investigated whether these metabolites contribute to the regulation of PD-L1 expression. This approach led to the discovery that treatment with either dimethyl fumarate (DMF), a cell-permeable

methyl ester that releases fumarate as well as itaconate or, to a lesser extent, succinate, robustly upregulate PD-L1 protein levels (Fig. 5E), while citrate had no effect (not shown).

Fumarate and itaconate promote non-enzymatic post-translational modifications of cysteine residues *via* succination, resulting in the activation or inhibition of downstream targets. One of the best-characterized targets of this reaction is Keap1 (Kelch-like ECH-associated protein 1), the substrate adaptor of the BCR (BTB-Cul3-RBX1) E3 ligase complex. Succination of Keap1 by fumarate leads to its degradation. Consistent with this mechanism, DMF treatment markedly reduced Keap1 protein levels, coinciding with PD-L1 upregulation (Fig. 5E). In addition, SLC25A1 over-expression decreased Keap1 levels (Fig. 5F). Conversely, SLC25A1 knockdown resulted in Keap1 upregulation (Fig. 5G). Finally, the Keap1 knockdown enhanced PD-L1 protein expression (Fig. 5H).

Thus, the results convincingly show that SLC25A1 enhances PD-L1 at least in part *via* TCA-cycle mediated downregulation of Keap1.

SLC25A1 induces the IFN-I response and PD-L1 expression *in vivo* and sensitizes to anti-PD-L1 blockade

Building upon the results from these previous *in vitro* studies, we next investigated whether SLC25A1 influences the response to PD-1/PD-L1 blockade. To accomplish this, we employed a syngeneic mouse model specifically the murine melanoma B16F0 cell line, a well-characterized and widely used model for studying immune checkpoint inhibitor (ICI) responses. Given the low basal, nearly undetectable expression of SLC25A1 in B16F0 cells, we employed naïve B16F0 cells, as well as the stable derivative cell line that restores SLC25A1 protein levels (see Fig. 1C). Control and SLC25A1^{high} cells were subcutaneously implanted into C57BL/6 mice, followed by treatment with either PD-L1-blocking antibodies or isotype control matched IgG, administered at 200 µg per mouse every three days for four doses once tumors became palpable. As amply reported in the literature, parental B16F0 tumors exhibited minimal, if any, responsiveness to PD-L1/PD-1 blockade (Fig. 6 A,B). Consistent with the previously described role of

SLC25A1 in promoting tumor growth, B16F0 cells stably expressing SLC25A1 had accelerated tumor growth rate compared to naïve cells. However, treatment with the PD-L1 antibody significantly suppressed the growth of SLC25A1^{high} tumors and reduced the incidence of progressing tumors in this group (Fig. 6 A,B).

Considering the identified SLC25A1-dependent induction of IFN-I in previously described *in vitro* models, we next assessed the expression of representative sets of ISGs in these tumors. As shown in Fig. 6 C, a robust activation of IFN-I downstream targets, OASL, ISG15, IFIT2 and STAT1 was observed in SLC25A1^{high} tumors treated with the PD-L1 antibody.

Importantly, Kaplan–Meier survival analysis using the KMplotter database demonstrated that high PD-L1 expression was significantly associated with improved overall survival in patients treated with anti–PD-L1 immune checkpoint blockade (atezolizumab or durvalumab) (Fig.7A). Patients with high PD-L1 expression exhibited a markedly prolonged survival probability compared with patients with low PD-L1 expression (HR = 0.44, 95% CI: 0.32–0.60; log-rank $P = 6.5 \times 10^{-8}$), indicating an approximately 56% reduction in the risk of death in the high-expression group. These findings support the notion that elevated SLC25A1 expression may identify tumors more responsive to PD-L1–targeted immunotherapy and are consistent with the concept that SLC25A1 levels can serve as a predictive biomarker of response to checkpoint blockade.

DISCUSSION

We have discovered a novel tumor-initiated immuno-regulatory program driven by SLC25A1 and by the mitochondria that through autocrine and paracrine activities converge on regulation of PD-L1 and on the induction of the IFN-I response (depicted in Fig. 7B). We first identified a novel molecular mechanism by which SLC25A1 induces a viral mimicry state and found that this induction is sustained by mtDNA, which in turn triggers activation of the IFN-I pathway. Second, SLC25A1 influences PD-L1 levels and, by investigating the molecular mechanisms underlying this cross-talk, we identified a previously unrecognized

mechanism regulating the expression of this protein, involving the activity of Keap1. Third, by employing syngeneic mouse models of tumor cells expressing high or low levels of Slc25a1, we show that melanoma xenografts with elevated SLC25A1 levels display a markedly improved response to PD-L1 blockade. Importantly, this enhanced response is associated with robust activation of ISGs. Therefore, the data are consistent with the hypothesis that SLC25A1 creates a tumor environment that is primed for tumor killing but acquires “immune privilege” *via* up-regulation of PD-L1 and thus, these tumors are uniquely sensitive to PD-L1 inhibition.

Recent pan-cancer and large scale analyses have further highlighted the clinical significance of SLC25A1 [. A recent study [47] further demonstrated that SLC25A1 is broadly over-expressed in multiple cancer types, as we originally showed [34,35,37], and that its high expression correlates with poor prognosis, higher tumor grade, and more advanced disease stage. Elevated SLC25A1 levels were also associated with variable immune cell infiltration, immune checkpoint expression, and increased tumor mutational burden, further suggesting that SLC25A1 contributes to shaping the tumor microenvironment, a possibility that had not been explored directly up to this point.

As discussed previously, the effects of IFN-I in the response to immunotherapy are complex and at times conflicting. Our data suggest that SLC25A1 creates a therapeutic vulnerability when tumor cells are treated with anti-PD-L1 antibody therapy, as a consequence of a potent IFN-I response together with enhanced PD-L1 expression. However, chronic IFN-I induction has also been associated with resistance to ICIs in some instances. Based on our findings, we propose that a quantitative, dose-dependent effect of the IFN-I gene program may be required to mediate tumor killing, and we posit that SLC25A1, and by promoting mitochondrial metabolism, acts by amplifying the magnitude of this response. However, considering the pro-survival activities exerted by a subset of ISGs, it is also possible that the outcome of SLC25A1 activity and of ICIs is qualitatively influenced by the composition of the ISG gene program in a more granular fashion. Dissecting the composition of this ISG response remains an important area of

ongoing investigation, and understanding which subsets of ISGs contribute to vulnerability *versus* resistance could allow for more precise therapeutic targeting.

Given that one major activity of SLC25A1 is the promotion of mitochondrial respiration [34], our data also raise the important question of whether drugs that stimulate mitochondrial OXPHOS might exert similar effects. Two such agents currently under investigation are dichloroacetate and fumarate, both of which are particularly attractive because they are already being evaluated in clinical trials. In addition, because tumor cells frequently exploit the PD-L1/PD1 axis and upregulate PD-L1 to evade anti-tumor immunity, there is considerable interest in understanding the mechanisms controlling PD-L1 stability. Indeed, elevated PD-L1 expression levels are often predictive of favorable clinical responses to ICIs; however, it is also documented that induction of PD-L1 degradation prevents immune escape and promotes recruitment of tumoricidal immune cells, thereby enhancing tumor killing in response to radio- or chemotherapy. In this respect, the identification of a novel pathway regulating PD-L1 expression levels involving both Keap1 and SLC25A1 provides an opportunity to rationally exploit Keap1- or SLC25A1-targeting agents to promote anti-tumor immune responses during conventional cancer therapies. Indeed, we have shown here that CTPI-2 significantly down-regulates PD-L1 expression in several tumor cell lines. We and others have also demonstrated that, in immuno-compromised mice, inhibition of the tumor-intrinsic activities of SLC25A1 using CTPI-2 or other SLC25A1 inhibitors synergizes with platinum therapy, radiotherapy, and EGFR-targeting agents [5]. In light of our discovery of tumor-extrinsic activities of SLC25A1 on the PD-L1 axis, these results now establish a rationale for inhibiting SLC25A1 in combination with canonical anti-tumor therapies to prevent adaptive PD-L1 upregulation following chemo- or radiotherapy. Therefore, overall, our data suggest that there may be therapeutic benefit in targeting SLC25A1 activity either positively, when anti-PD-L1 represents the primary treatment, or negatively, when chemotherapy or targeted therapies are employed.

Additionally, and in keeping with the broader pro-oncogenic roles played by inflammation, it is possible that the inflammatory response triggered by SLC25A1 ultimately favors an oncogenic program that drives

tumor development, reflecting the dual nature of inflammation in cancer in both enabling tumor growth and creating therapeutic vulnerabilities.

Materials and Methods

Cells, reagents and antibodies

The H1299, B16F0, and HCC1937 cell lines were sourced from ATCC or the Tissue Culture Shared Resource at the Georgetown University Lombardi Comprehensive Cancer Center (LCCC) as previously described [36,52]. The 293T cells were provided by Dr. Chunling Yi, whereas HCC827 and H1975 cells were provided by Dr. Giuseppe Giaccone. The patient-derived NSCLC lines have been reported previously [34]. Cells were maintained in high-glucose DMEM containing 25 mM glucose, glutamine, and pyruvate (Invitrogen), supplemented with 10% fetal bovine serum and 1% penicillin–streptomycin stock solution (5,000 units/mL; Gibco). CTPI-2 (PubChem; CAS 68003-38-3) was obtained from Enamine Ltd. Other compounds included cyclosporine A (Cell Signaling, 9973), ethidium bromide (Alfa Aesar, J62282), dimethyl fumarate (Sigma, 242926), dimethyl succinate (Sigma, W239607), dimethyl malate (Sigma, 374318), MG132 (Sigma, 474790), and chloroquine (MP Biomedicals, 193919). Human SLC25A1 (OriGene, SC120727) and FLAG-tagged PD-L1 (Sino Biological, HG10084-NF) expression vectors were used. Sigma supplied the shRNA constructs targeting SLC25A1 (TRCN0000232825), cGAS (TRCN0000149984), STAT1 (TRCN0000280021), IFNAR (TRCN0000059013), and KEAP1 (TRCN0000154657). SLC25A1 was detected by immunoblotting with antibodies from either Santa Cruz Biotechnology (sc-86392) or Proteintech (15235-1-AP). The remaining immunoblotting antibodies recognized PD-L1 (GeneTex, GTX104763), KEAP1 (Proteintech, 10503-2-AP), OPA1 (Novus Biologicals, NB110-55290), cGAS (Cell Signaling, 15102), STAT1 (Cell Signaling, 14994), IFIT2 (Proteintech, 12604-1-AP), β-actin (Santa Cruz Biotechnology, sc-47778), and HSP70 (Santa Cruz Biotechnology, sc-7298).

Growth of monolayer and sphere cultures

Adherent and three-dimensional cultures were generated as reported previously [34,36,52]. Tumor cells grown as monolayers were maintained in DMEM (Gibco) supplemented with 10% fetal bovine serum and

1% penicillin–streptomycin stock (5,000 units/mL; Gibco). To promote spheroid growth, cells were transferred to Falcon bacteriological Petri dishes precoated with 2% poly(2-hydroxyethyl methacrylate) dissolved in absolute ethanol. Spheroid medium consisted of DMEM/F12 (Gibco) containing 20 ng/mL epidermal growth factor, 5 ng/mL fibroblast growth factor, 0.375% N2 supplement from a 100× stock (Gibco), and 1% penicillin–streptomycin. Single-cell suspensions were prepared with 0.25% trypsin–EDTA (Gibco) for monolayers and StemPro Accutase (Gibco) for spheroids.

Inhibition of SLC25A1 activity

SLC25A1 was pharmacologically inhibited by treating monolayer or spheroid cultures with CTPI-2 at 50 or 100 μM for 24 or 48 h. CTPI-2 stock solutions were prepared in DMSO.

Gene expression profiling of SLC25A1 over-expressing or control H1299 cells grown in monolayers or spheres conditions

Poly(A)-selected RNA was purified from each sample and processed to generate labeled cRNA according to the Agilent Technologies protocol. The cRNA was hybridized to SurePrint G3 Human Gene Expression v3 8 × 60K Microarrays (Agilent Technologies, Santa Clara, CA, USA), which were subsequently scanned with a SureScan system. Probe-level signals were consolidated by gene and subjected to background correction and quantile normalization with the R package limma. Samples and genes were hierarchically clustered using Manhattan distance and Ward linkage. Gene-set enrichment analysis was performed with the R package fgsea.

Immunoblots of cells and murine tumor tissues

Immunoblotting was conducted using a previously described protocol [32]. Adherent cells were collected by scraping, whereas spheroid cultures were recovered by centrifugation. Frozen tumor tissues were pulverized under liquid nitrogen using a mortar and pestle. Cells and tissue powders were lysed in RIPA buffer containing cOmplete Mini Protease Inhibitor Tablets (Roche, 11836153001). Protein concentrations were measured with the Coomassie Bradford Protein Assay Kit (Pierce), and equivalent protein quantities

were resolved on Novex 4–20% Tris–glycine gels (Invitrogen). Following transfer to PVDF membranes, nonspecific binding was blocked with buffer containing 10% horse serum. Membranes were incubated sequentially with the indicated primary antibodies and the appropriate horseradish peroxidase-conjugated secondary antibodies (Invitrogen). Signals were detected using SuperSignal West Pico PLUS Chemiluminescent Substrate (Thermo Scientific). β-Actin or HSP70 served as loading controls.

Quantitative real-time PCR

qRT-PCR was performed as previously described [52]. Total RNA was extracted using TRIzol® (Thermo Scientific) and incubated with DNase I and SUPERase•In™ RNase Inhibitor (Thermo Scientific) for 30 min at 37 °C. DNase activity was terminated by adding EDTA to 5 mM and heating at 75 °C for 10 min. Following supplementation with 5 mM $MgCl_2$, cDNA was synthesized from random hexamers using SuperScript™ IV according to the manufacturer's protocol. Quantitative real-time PCR was performed with PowerUp™ SYBR® Green Master Mix (Thermo Scientific). Human transcript levels were normalized to two of three reference genes (GAPDH, SNRPD3, and TBP), whereas murine transcripts were normalized to two of Actb, Ppia, and Tbp. Relative expression was determined by the ΔΔCt method. Primer specificity was confirmed by dissociation-curve analysis, which yielded a single amplification product, and no-reverse-transcriptase controls were included to exclude genomic DNA contamination.

Sorting of $CD133^+$ and $CD44^+/CD24^-$ CSCs

SLC25A1-overexpressing H1299 cells were cultured as spheroids for 3 days to enrich for cancer stem cells (CSCs) [52]. Spheroids were collected by centrifugation, dissociated into single cells, washed with PBS, and resuspended in DMEM. CD133-positive and CD133-negative populations were identified using APC-conjugated anti-human CD133 antibody (BioLegend, #372806). CD44-positive/CD24-negative cells were identified by co-staining with APC-conjugated anti-mouse/human CD44 (BioLegend, #103012) and PE-conjugated anti-human CD24 (BioLegend, #311106) antibodies. Following incubation for 30 min at 37 °C, cells were washed three times, resuspended in DMEM, and sorted by the Georgetown University

Lombardi Comprehensive Cancer Center core facility. RNA was subsequently extracted from the sorted populations, and ISG expression was quantified by qRT-PCR.

Quantification of mtDNA levels in pure cytosolic fractions

StemPro Accutase (Gibco) was used to disperse spheroids into single cells, which were washed, counted, and suspended in PBS at 5 × 10^6 cells per 500 µL [52]. One-fifth of the suspension was reserved for mtDNA normalization. This aliquot was pelleted, incubated in 500 µL of 50 µM NaOH for 30 min with heating, and neutralized with 50 µL of 1 M Tris-HCl (pH 8.0) before measurement of total cellular mtDNA. The remaining cells were collected and gently suspended in 500 µL of buffer containing 150 mM NaCl, 50 mM HEPES (pH 7.4), and 20 µg/mL digitonin (Sigma, D141). Selective plasma-membrane permeabilization was achieved by end-over-end mixing for 10 min at room temperature. Intact cells were cleared by three sequential centrifugations at 980 × g for 3 min, transferring the supernatant to a fresh tube after each spin; the initial pellet was retained for immunoblotting. The final supernatant was centrifuged at 17,000 × g for 10 min to eliminate residual cellular debris.

Depletion of mtDNA using EtBr. To generate mtDNA-depleted cells, adherent cultures were exposed to 150 ng/mL ethidium bromide (EtBr) for 3 days [52]. The EtBr-containing medium was then removed, and cells were trypsinized and transferred to spheroid-forming conditions. After sphere formation, spheroids were collected by centrifugation and dissociated with StemPro Accutase (Gibco). Cells were suspended in PBS, and equivalent numbers of control and EtBr-treated cells were collected. Each sample was lysed in 500 µL of 50 µM NaOH by heating for 30 min to release and solubilize DNA. mtDNA depletion was verified by quantitative PCR using primer pairs targeting the mitochondrial CYTB, ND2, and 16S sequences, with the nuclear GAPDH gene serving as the normalization control. Mitochondrial target Ct values were normalized to the corresponding GAPDH Ct values. The nuclear genes SNRPD3 and TBP were also analyzed by qRT-PCR to confirm that EtBr treatment did not affect genomic DNA.

Conditioned culture supernatants experiment

Conditioned medium was collected after culturing control or SLC25A1-overexpressing H1299 spheroids for 3 days. Adherent HCC827 recipient cells were incubated overnight with unconditioned spheroid medium or medium conditioned by either H1299 spheroid population. HCC827 cells were then harvested, and PD-L1 protein abundance was evaluated by immunoblotting [52].

TCA metabolites treatments

Adherent H1299 cultures were established overnight and subsequently exposed to dimethyl malate, dimethyl succinate, or dimethyl fumarate for an additional overnight period. Untreated and metabolite-treated cells were then collected, and PD-L1 protein levels were assessed by immunoblotting.

Tumor xenografts experiments and ICIs treatment

Control and SLC25A1-overexpressing B16F0 cells were maintained for 3 days under spheroid-forming conditions in DMEM/F12 supplemented with 2.5% KnockOut™ Serum Replacement (Gibco), 1% glutamine, 1% 100× ITS solution (Sigma, I3146), 1% sodium pyruvate, 0.1% Y-compound, and 1% penicillin–streptomycin [36,52] The resulting spheroids were enzymatically dispersed with StemPro Accutase (Gibco), suspended as single cells in PBS, and assessed for cell number and viability. Five-week-old female wild-type C57BL/6J mice obtained from The Jackson Laboratory received bilateral subcutaneous injections of 5×10^5 viable control or SLC25A1-overexpressing cells into the lower flanks. Three independent experiments were performed using 5-6 mice per treatment group (mean n = 5.25 mice/group/experiment). Across the three experiments, the cumulative n was 15-20 mice for each of the experimental groups. After tumors became palpable, animals within each tumor group were randomized to treatment with either an anti-mouse PD-L1 antibody (Bio X Cell, BE0101) or a rat IgG2b anti-keyhole limpet hemocyanin isotype control (Bio X Cell, BE0090). Antibodies were administered intraperitoneally at 200 µg per mouse every 3 days for four total doses. Tumor dimensions were monitored with digital calipers, and volumes were calculated as length × width × height × 0.523. Animals were euthanized when tumors reached the maximum permitted volume, after which tumors were excised for further analysis. Euthanasia was performed by carbon dioxide inhalation, followed by cervical dislocation to confirm death. All

procedures were conducted under a protocol approved by the Georgetown University Institutional Animal Care and Use Committee.

Immunohistochemistry

Immunohistochemistry was performed on formalin-fixed, paraffin-embedded sections of control and SLC25A1-overexpressing B16F0 tumors using our previously described protocol. Briefly, 5-μm tissue sections were deparaffinized in xylene and rehydrated through a graded series of alcohol solutions. Heat-induced epitope retrieval was conducted in Target Retrieval Solution, Low pH, using a PT Link system (DAKO). The sections were sequentially treated with 3% hydrogen peroxide, avidin/biotin blocking reagents, and 10% normal goat serum. Mouse PD-L1 was detected by incubating the sections for 1 hour at room temperature with a rabbit polyclonal anti-mouse PD-L1 antibody (ABclonal, A1645). Consecutive sections processed without the primary antibody served as negative controls. Stained slides were scanned using a Vectra 3 multispectral imaging microscope and analyzed with Vectra and Phenochart software (PerkinElmer).

Generation of graphical images. Generative AI tools were used exclusively for the generation of the graphic abstract included in the submission.

Statistics

Statistical analyses were performed using GraphPad Prism. Comparisons between groups were conducted using analysis of variance and paired or unpaired two-tailed Student's t tests, as appropriate. Differences were considered statistically significant at $P \leq 0.05$. Significance is indicated as follows: $^{*}P \leq 0.05$, $^{**}P \leq 0.01$ and $^{***}P \leq 0.001$.

Authors contribution. MLA designed most of the experiments and wrote the paper. RM designed several experiments, proof edited the manuscript for accuracy, performed the majority of the experiments, and organized the data for the Figures. MM helped performing the in vivo experiments and MC provided

important inputs for interpretation. AK and SP performed some of the experiments in the patient-derived cell lines and CA contributed to the editing and development of the in vivo experiments.

Funding. Studies on SLC25A1 in the MLA lab have been supported by R01CA193698, R21DE028670, R21CA256546 and R03TR004871. All these studies have been supported by the outstanding facility at GUMC and by the 2P30CA051008-30 CCSG grant.

Ethic Statements.

Conflict of Interest. The authors declare that they have no known competing financial interests or personal relationships that could have appeared to influence the work reported in this paper.

Ethic Approval and Consent to Participate. All animal studies were conducted in compliance with ethical regulations according to protocol #2017-1192 approved by the Institutional Animal Care and Use Committee (IACUC) at Georgetown University. All the mice were housed at Georgetown University Division of Comparative Medicine, in a SPF vivarium which is maintained at a 12:12 h light:dark cycle, at 68–74°F and 30–70% humidity range, according to IACUC regulations. For tumor bearing mice, tumors were measured with caliper and maximum allowable tumor size as per IACUC regulations is 1.5 cm for single tumors and 1 cm for double tumors, and not to exceed 10% of total body weight.

At the experimental endpoint, mice remained in their home cage to minimize handling-associated distress. The cage was fitted with a dedicated CO_2 delivery lid connected by tubing to a compressed-CO_2 cylinder equipped with a pressure regulator and flow meter. CO_2 was introduced gradually at a rate that displaced 30–70% of the cage volume per minute. Exposure continued until complete cessation of respiration and movement, and the mice remained in the cage for a minimum of 5 minutes. Cervical dislocation was subsequently performed as a secondary physical method to confirm death, in accordance with the Georgetown University IACUC-approved procedure.

This study did not involve the prospective recruitment of human participants or the collection of new human specimens. The patient-derived samples used in this study were collected and approved as previously described [34]. All samples and associated data were de-identified before being provided to the investigators, and the investigators remained blinded to patient identity throughout the study. No information capable of identifying individual patients was accessed or analyzed.

Data Availability. All data generated or analyzed in this study, including the GraphPad Prism files are available from the corresponding author upon reasonable request. The patient-derived data consist of the immunoblot results presented in the manuscript; no additional identifiable patient-level data were generated or analyzed.

Acknowledgements. We are grateful to Dr. Harvey Fernandez, as well as to Anton Wellstein for many inputs on this project, to the Riegel/Wellstein and to Dr. Chunling Yi laboratories for sharing reagents and instrumentation. We also thank Dr. Giuseppe Giaccone, Dr. Pacini and Dr. Petrini, for the sharing of the patient-derived cell lines which were also described previously [34].

REFERENCES

1. Sharma P, Hu-Lieskovan S, Wargo JA, Ribas A. Immune checkpoint therapy-current perspectives. Science 2023;374

2. Jiang Y, Chen M, Nie H, Yuan Y. PD-1 and PD-L1 in cancer immunotherapy: clinical implications and future considerations. Hum Vaccin Immunother 2019;15:1111–1122.

3. Wei SC, Duffy CR, Allison JP. Fundamental mechanisms of immune checkpoint blockade therapy. Cancer Discov 2018;8:1069–1086.

4. Petitprez F, Meylan M, de Reyniès A, Sautès-Fridman C, Fridman WH. The tumor microenvironment in the response to immune checkpoint blockade therapies. Front Immunol 2020;11:784.

5. Morad G, Helmink BA, Sharma P, Wargo JA. Hallmarks of response, resistance, and toxicity to immune checkpoint inhibitors. Cell 2021;184:5309–5327

6. Gibney GT, Weiner LM, Atkins MB. Predictive biomarkers for checkpoint inhibitor-based immunotherapy. Lancet Oncol 2016;17:e542–e551.

7. Yarchoan M, Albacker LA, Hopkins AC, et al. PD-L1 expression and tumor mutational burden are independent biomarkers of response to immune checkpoint inhibitors. J Clin Invest 2019;129:3374–3382.

8. Li H, Wang J, Huang L, et al. Biomarkers of response to PD-1 pathway blockade: evaluating PD-L1 expression as a predictor of ICI efficacy. Br J Cancer 2022;126:19–29.

9. Schaer DA, Beckmann RP, Dempsey JA, Huber L, Forest A, Amaladas N, et al. The CDK4/6 inhibitor abemaciclib induces a T cell-inflamed tumor microenvironment and enhances the efficacy of PD-L1 checkpoint blockade. Cell Reports 2018;22:2978–2994.

10. Zhang J, Bu X, Wang H, Zhu Y, Geng Y, Nihira NT, et al. Cyclin D-CDK4 kinase destabilizes PD-L1 via Cul3SPOP to control cancer immune surveillance. Nature 2018;553:91–95.

11. Gou Q, Dong C, Xu H, Khan B, Jin J, Liu Q, et al. PD-L1 degradation pathway and immunotherapy for cancer. Cell Death Dis 2020;11:955

12. Aricò E, Castiello L, Capone I, Gabriele L, Belardelli F. Type I interferons and cancer: an evolving story demanding novel clinical applications. Cancers (Basel) 2019;11:1943.

13. Zemek RM, De Jong E, Chin WL, Schuster IS, Fear VS, Casey TH, et al. Sensitizing the tumor microenvironment to immune checkpoint therapy. Front Immunol 2020;11:223.

14. Medrano RFV, Hunger A, Mendonça SA, Barbuto JAM, Strauss BE. Immunomodulatory and antitumor effects of type I interferons and their application in cancer therapy. Oncotarget 2017;8:71249–71284.

15. Minn AJ, Wherry EJ. Combination cancer therapies with immune checkpoint blockade: convergence on interferon signaling. Cell 2016;165:272–275.

16. Teijaro JR. Type I interferons in viral control and immune regulation. Curr Opin Virol 2016;16:31–40

17. Qadir AS, Ceppi P, Brockway S, Law C, Mu L, Khodadadi-Jamayran A, et al. CD95/Fas increases stemness in cancer cells by inducing a STAT1-dependent type I interferon response. Cell Rep 2017;18:2373–2386.

18. Erdal E, Haider S, Rehwinkel J, Harris AL, McHugh PJ. A prosurvival DNA damage-induced cytoplasmic interferon response is mediated by end resection factors and is limited by Trex1. Genes Dev 2017;31:353–369.

19. Weichselbaum RR, Ishwaran H, Yoon T, Nuyten DS, Baker SW, Khodarev N, et al. An interferon-related gene signature for DNA damage resistance is a predictive marker for chemotherapy and radiation for breast cancer. Proc Natl Acad Sci U S A 2008;105:18490–18495.

20. Benci JL, Xu B, Qiu Y, Wu TJ, Dada H, Twyman-Saint Victor C, et al. Tumor interferon signaling regulates a multigenic resistance program to immune checkpoint blockade. Cell 2016;167:1540–1554.e12.

21. Benci JL, Johnson LR, Choa R, Xu Y, Qiu J, Zhou Z, et al. Opposing functions of interferon coordinate adaptive and innate immune responses to cancer immune checkpoint blockade. Cell 2019;178:933–948.e14.

22. Guo J, Zhou J, Yuan Y, Huang Y, Yang J, Qiu Y, et al. Empowering therapeutic antibodies with IFN-α for cancer immunotherapy. PLoS One 2019;14:e0219829.

23. Romero D. Interferon enhances immune-checkpoint inhibition. Nat Rev Clin Oncol 2019;16:6.

24. Zhu Y, Tibensky I, Schmidt J, Ryschich E, Märten A. Interferon-α enhances antitumor effect of

25. chemotherapy in an orthotopic mouse model for pancreatic adenocarcinoma. J Immunother

26. 2008;31:599–606.

27. Harel M, Ortenberg R, Varanasi SK, Mangalhara KC, Mardamshina M, Markovits E, et al. Proteomics of melanoma response to immunotherapy reveals mitochondrial dependence. Cell 2019;179:236–250.e18.

28. Gonzalez-Cao M, Iduma P, Karachaliou N, Santarpia M, Blanco J, Rosell R. Activation of viral defense signaling in cancer. Ther Adv Med Oncol 2018;10:1758835918793108.

29. Deblois G, Smith HW, Tam IS, Gravel SP, Caron M, Savage P, et al. Epigenetic switch–induced viral mimicry evasion in chemotherapy-resistant breast cancer. Cancer Discov 2020;10:1312–1329.

30. Roulois D, Loo Yau H, Singhania R, Wang Y, Danesh A, Shen SY, et al. DNA-demethylating agents target colorectal cancer cells by inducing viral mimicry by endogenous transcripts. Cell 2015;162:961–973.

31. Formenti SC, Rudqvist NP, Golden E, Cooper B, Wennerberg E, Lhuillier C, et al. Radiotherapy induces responses of lung cancer to CTLA-4 blockade. Nat Med 2018;24:1845–1851.

32. Won JK, Bakhoum SF. The cytosolic DNA-sensing cGAS–STING pathway in cancer. Cancer Discov 2020;10:26–39.

33. Bakhoum SF, Ngo B, Laughney AM, Cavallo JA, Murphy CJ, Ly P, et al. Chromosomal instability drives metastasis through a cytosolic DNA response. Nature 2018;553:467–472.

34. Kasprzyk-Pawelec A, Tan M, Rahhal R, McIntosh A, Fernandez HR, Mosaoa RM, Jiang L, Pearson GW, Glasgow E, Vockley J, Albanese C, Avantaggiati ML. Inactivation of the SLC25A1 gene during embryogenesis induces a unique senescence program controlled by p53. Cell Death Differ 2025;32:818–836.

35. Mosaoa R, Kasprzyk-Pawelec A, Fernandez HR, Avantaggiati ML. The mitochondrial citrate carrier SLC25A1/CIC and the fundamental role of citrate in cancer, inflammation and beyond. Biomolecules 2021;11:141.

36. Fernandez HR, Gadre SM, Tan M, Graham GT, Mosaoa R, Ongkeko MS, et al. The mitochondrial citrate carrier, SLC25A1, drives stemness and therapy resistance in non-small cell lung cancer. Cell Death Differ 2018;25:1239–1258.

37. Catalina-Rodriguez O, Kolukula VK, Tomita Y, Preet A, Palmieri F, Wellstein A, et al. The

38. mitochondrial citrate transporter, CIC, is essential for mitochondrial homeostasis. Oncotarget

39. 2012;3:1220–1235.

40. Butow RA, Avadhani NG. Mitochondrial signaling: the retrograde response. Mol Cell 2004;14:1–15.

41. Liu Z, Butow RA. Mitochondrial retrograde signaling is a pathway of communication from mitochondria to the nucleus under normal and pathophysiological conditions. Annu Rev Genet 2006;40:159–185.

42. Bhat N, Fitamant J, Hauck L, et al. Recognition of cytosolic DNA by cGAS and other STING pathway sensors. *Nat Rev Immunol* 2014;14:76–88.

43. Kong LZ, Xue WJ, Wang ZH, et al. Understanding nucleic acid sensing and its therapeutic opportunities. *Mol Cancer* 2023;22:180.

44. Wu Z, Bogardus H, Safaee Modaress S, Esposito D, Caveloo H, Shadel GS. Mitochondrial DNA stress signalling protects the nuclear genome. Nat Commun 2019;10:5646.

45. Sun C, Mezzadra R, Schumacher TN. Regulation and function of the PD-L1 checkpoint. Immunity 2018;48:434–452.

46. Jiang X, Wang J, Deng X, Xiong F, Ge J, Xiang B, et al. Role of the tumor microenvironment in PD-L1/PD-1-mediated tumor immune escape. Mol Cancer 2019;18:10.

47. Cha JH, Chan LC, Li CW, Hsu JL, Hung MC. Mechanisms controlling PD-L1 expression in cancer. Mol Cell 2019;76:359–370.

48. Chen J, Chen Z, Chen M, Liu H, Luo Y, Xu L, et al. Tumor cell-derived lactate induces TAZ-dependent upregulation of PD-L1. Oncogene 2017;36:5829–5839.

49. Ajina R, Malchiodi ZX, Fitzgerald AA, Zuo A, Wang S, Moussa M, et al. Antitumor T-cell immunity contributes to pancreatic cancer immune resistance. Cancer Immunol Res 2021;9:386–400.

50. Nasrollahzadeh E, Rahbarizadeh F, Ahmadvand D, Hartmann T. Pro-tumorigenic functions of macrophages at the primary, invasive and metastatic tumor site. Cancer Immunol Immunother 2020;69:1673–1697.

51. You Y, Wu Y, Chen Y, Fang H, Xu Y, Dai Y, Zhang J, Wu S. A comprehensive analysis of SLC25A1 expression and its prognostic potential in cancers. *Front Oncol*. 2023;13:1224995.

52. Mosaoa, Rami M. *Role of the Mitochondrial Citrate Transporter, Slc25a1, In Cancer, Obesity and Liver Steatosis.* Biochemistry and Molecular Biology, 2021. hdl.handle.net/10822/1062301

Figure Legends

Fig. 1: An immune-related signature is activated in SLC25A1-expressing NSCLC and melanoma spheroids.

A. Immuno-histochemistry (IHC) of SLC25A1 in NSCLCs derived tumors. Squares indicate enlarged tumors shown in panels 1, 2 and 3.

B. SLC25A1 levels in normal (N) tumor (T) tissues derived from patients with NSCLCs.

C. Protein expression levels of SLC25A1 in H1299 and B16F0 cells naive (low), or expressing exogenous SLC25A1 (high). Results are representative of 3 independent experiments.

D. Gene set enrichment analysis (GSEA) of microarray experiments revealed significant enrichment of immune- and metabolism-related pathways in SLC25A1^{high} versus H1299-SLC25A1^{low} spheroids (n=3 per each group). Bars represent enriched gene sets ranked by statistical significance (–log10 *p*-value). Pathways associated with interferon signaling, immune checkpoint regulation, and T cell responses are highlighted in red.

E. Heatmap of most enriched genes in H1299 control or SLC25A1-expressing spheres representing the ISGs. In red are the genes validated in this study with qRT-PCR or immunoblot.

Figure 2. SLC25A1 conveys an IFN-I antiviral response.

A. Fold change in gene expression of the indicated ISGs in the indicated H1299 spheres.

B. Fold change in gene expression of the indicated ISGs in B16F0 spheres

C. Levels of c-GAS, STAT1 and □-Actin in SLC25A1 H1299 low and high cells.

D-E. Fold change in gene expression of the indicated ISGs in $CD44^{+}/CD24^{-}$ CSCs (D), or $CD133^{+}$ (E) CSCs that were isolated from $SLC25A1^{high}$ spheres, relative to control negative populations.

All experiments were performed multiple times (n=3-5).

The error bars represent standard deviations, asterisks refer to $*p \leq 0.05$; $**p \leq 0.01$; $***p \leq 0.001$ by unpaired *T*-test.

Figure 3. **Cytosolic mtDNA accumulation drives the IFN-I response.**

A-B. Levels of mtDNA in the cytosolic fractions of $SLC25A1^{high}$ H1299 (A) and T293 (B) cells (red, n=3) relative to control cells (blue, n=3).

C. Fold change in gene expression of the indicated ISGs in $SLC25A1^{high}$ H1299 spheres treated with CsA (red, n=3) relative to control untreated spheres (blue, n=3-4).

D. Ratio of mtDNA to genomic DNA *(GAPD H*) measured by q-PCR on total extract of $SLC25A1^{high}$ H1299 cells treated with EtBr (red, n=3) relative to control untreated cells (blue, n=3).

E. Levels of mtDNA (16S and ND2) in the cytosolic fraction of $SLC25A1^{high}$ H1299 cells treated with EtBr (red, n=3) relative to control untreated cells (blue, n=3).

F. Fold change in gene expression of the indicated ISGs in $SLC25A1^{high}$ H1299 spheres treated with EtBr (red, n=3) relative to untreated control spheres (blue, n=3).

G. Schematic representation of the SLC25A1-IFN pathway and of the components that we found regulated (indicated in red).

The error bars represent standard deviations, asterisks refer to $*p \leq 0.05$; $**p \leq 0.01$; $***p \leq 0.001$ by unpaired *T*-test.

Figure 4. SLC25A1 induces PD-L1 expression in a cell intrinsic and extrinsic fashion.

A. Schematic representation of the experiments.

B-D. PD-L1 and SLC25A1 protein levels in control and $SLC25A1^{high}$ H1299 spheres (B), or in spheres treated with CTPI-2 (C), or transduced with the SLC25A1 shRNA (D).

E. PD- L1 and SLC25A1 protein levels in the indicated tumor (H1975 and HCC1937) and patient-derived (T5) NSLCs untreated or treated with CTPI-2.

F. PD-L1 and SLC25A1 protein levels in HCC827 cells treated with control media, or with conditioned culture supernatant derived from SLC25A1^{low} or SLC25A1^{high} spheres.

Figure 5. **Induction of PD-L1 by fumarate and Keap1.**

A. PD-L1 protein levels in control or EtBr-treated H1299 spheres used at two different concentrations (indicated by +).

B. PD-L1 protein levels in SLC25A1^{high} H1299 spheres infected with control lentivirus (pLKO) or with pLKO lentivirus harboring the shRNA for IFNAR1.

C-D. Effects of the knock-down of cGAS or STAT1 on PD-L1 mRNA (C) or protein (D) levels in SLC25A1^{high} H1299 spheres. In D, two different exposures of the PD-L1 blot are shown (Exp. 1 and 2).

E. Treatment of naïve H1299 with fumarate (DMF), itaconate, succinate and malate for 16 hours and immuno-blot with the indicated proteins.

F-G. Keap1, PD-L1 and SLC25A1 protein levels in SLC25A1^{high} H1299 (F) or harboring the SLC25A1 shRNA (G).

H. Keap1, PD-L1 and SLC25A1 protein levels in H1299 in spheres harboring control or the Keap1 shRNA.

Figure 6. SLC25A1 influences the response to anti-PD-L1 antibody therapy.

A. Tumor volumes and total number of tumors for the indicated treatment groups from three independent experiments (n=4-6 mice per group in each experiment).

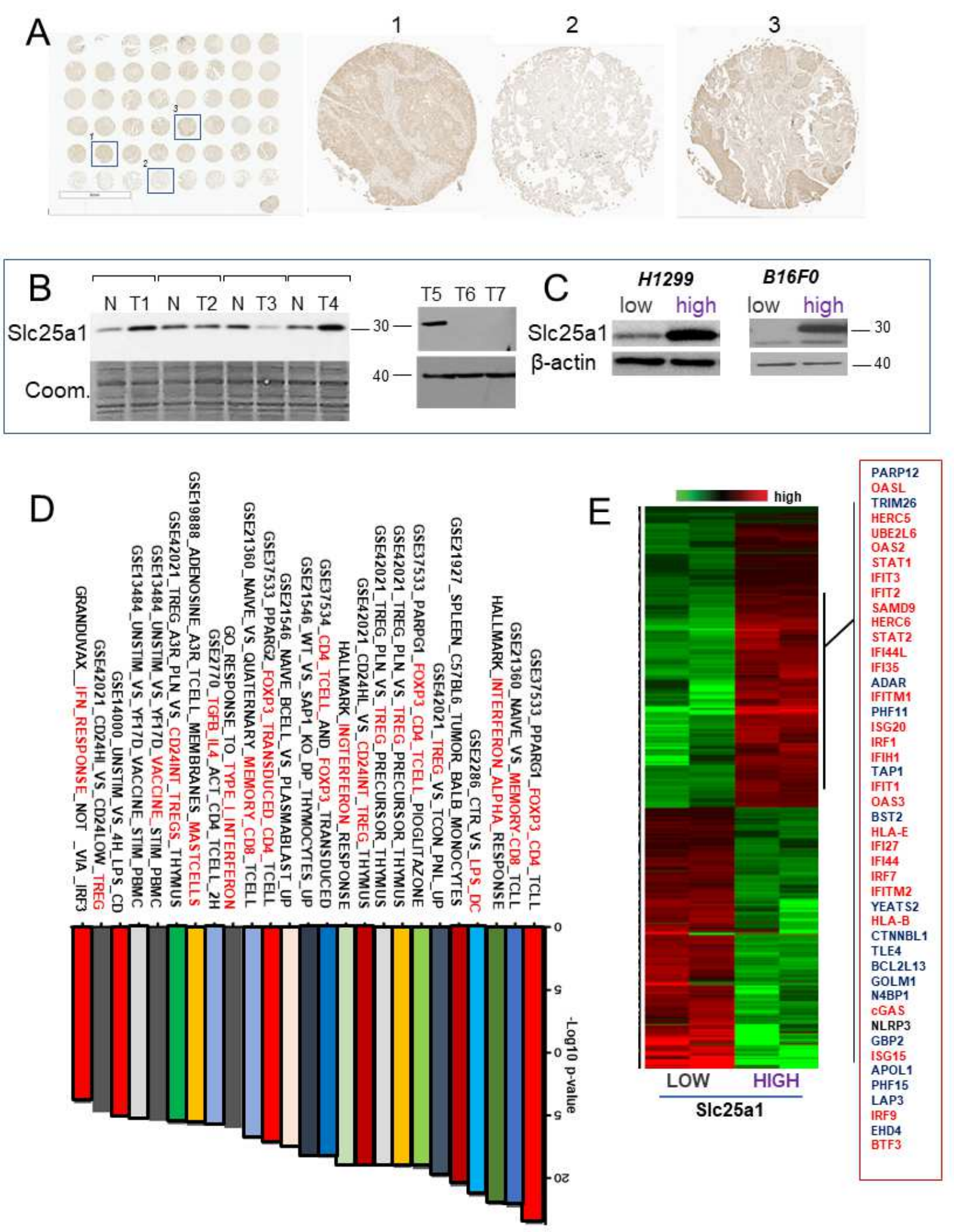
B. Tumor growth curves of control and SLC25A1 over-expressing B16F0 tumors treated with either PD-L1 (αPD-L1) or isotype control antibodies.

C. q-RT-PCR of the indicated IFN-I markers. Asterisks refer to $*p \leq 0.05$; $**p \leq 0.01$; ** $*p \leq 0.001$ by unpaired *T*-test.

Figure 7. SLC25A1-Dependent Regulation of PD-L1 Activity and Association with Response to Anti–PD-L1 Immunotherapy.

A. Kaplan–Meier overall survival curves of patients receiving anti-PD-L1 immune checkpoint therapy (atezolizumab or durvalumab) stratified according to PD-L1 expression levels using the KMplotter database. High PD-L1 expression was associated with significantly improved survival compared with low PD-L1 expression (HR = 0.44, 95% CI: 0.32–0.60; log-rank $P = 6.5 \times 10^{-8}$). No significant association was observed in patients treated with anti–PD-1 therapies.

B. Proposed model of the tumor-intrinsic immunoregulatory program driven by SLC25A1, involving mitochondrial signaling, regulation of PD-L1 expression, and activation of the type I interferon response (see also text). *Created with Biorender*.


A
1
2
3
B
N T1 N T2 N T3 N T4
T5 T6 T7
Slc25a1
Coom.
30
40
C
H1299
B16F0
low high
low high
Slc25a1
β-actin
30
40
D
GSE37533_PPARG1_FOXP3_CD4_TCLL
GSE21360_NAIVE_VS_MEMORY_CD8_TCLL
HALLMARK_INTERFERON_ALPHA_RESPONSE
GSE2286_CTR_VS_LPS_DC
GSE21927_SPLEEN_C57BL6_TUMOR_BALB_MONOCYTES
GSE42021_TREG_VS_TCON_PNL_UP
GSE37533_PARPG1_FOXP3_CD4_TCELL_PIOGLITAZONE
GSE42021_TREG_PLN_VS_TREG_PRECURSOR_THYMUS
GSE42021_TREG_PLN_VS_TREG_PRECURSOR_THYMUS
GSE42021_CD24HL_VS_CD24INT_TREG_THYMUS
HALLMARK_INGTERFERON_RESPONSE
GSE37534_CD4_TCELL_AND_FOXP3_TRANSDUCED
GSE21546_WT_VS_SAP1_KO_DP_THYMOCYTES_UP
GSE21546_NAIVE_BCELL_VS_PLASMABLAST_UP
GSE37533_PPARG2_FOXP3_TRANSDUCED_CD4_TCELL
GSE21360_NAIVE_VS_QUATERNARY_MEMORY_CD8_TCELL
GO_RESPONSE_TO_TYPE_I_INTERFERON
GSE2770_TGFB_IL4_ACT_CD4_TCELL_2H
GSE19888_ADENOSINE_A3R_TCELL_MEMBRANES_MASTCELLS
GSE42021_TREG_A3R_PLN_VS_CD24INT_TREGS_THYMUS
GSE13484_UNSTIM_VS_YF17D_VACCINE_STIM_PBMC
GSE13484_UNSTIM_VS_YF17D_VACCINE_STIM_PBMC
GSE14000_UNSTIM_VS_4H_LPS_CD
GSE42021_CD24HI_VS_CD24LOW_TREG
GRANDUVAX__IFN_RESPONSE_NOT _VIA_IRF3
0
5
0
5
20
-Log10 p-value
E
high
LOW
HIGH
Slc25a1
PARP12
OASL
TRIM26
HERC5
UBE2L6
OAS2
STAT1
IFIT3
IFIT2
SAMD9
HERC6
STAT2
IFI44L
IFI35
ADAR
IFITM1
PHF11
ISG20
IRF1
IFIH1
TAP1
IFIT1
OAS3
BST2
HLA-E
IFI27
IFI44
IRF7
IFITM2
YEATS2
HLA-B
CTNNBL1
TLE4
BCL2L13
GOLM1
N4BP1
cGAS
NLRP3
GBP2
ISG15
APOL1
PHF15
LAP3
IRF9
EHD4
BTF3

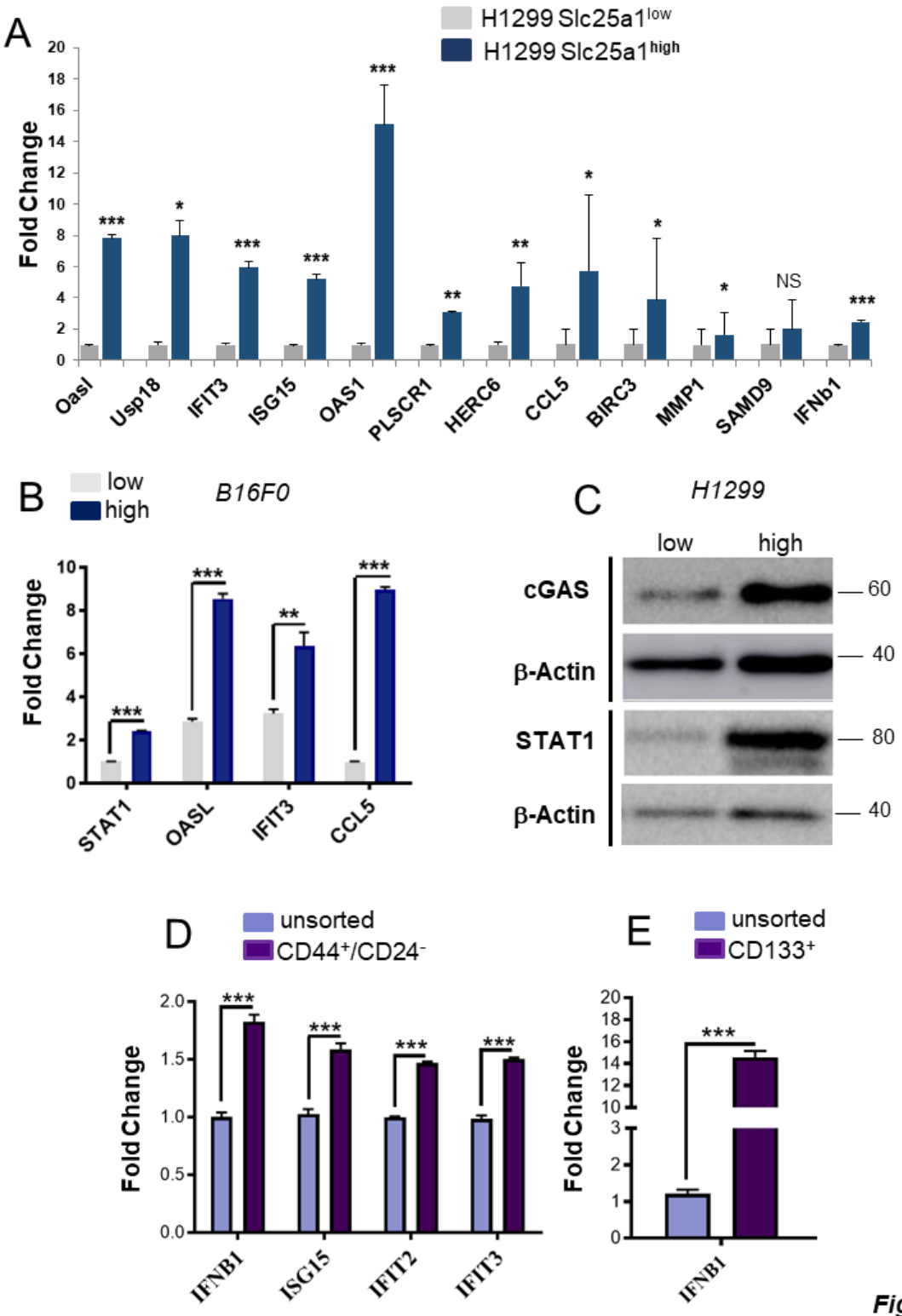

A
H1299 Slc25a1low
H1299 Slc25a1high
Fold Change
Oasl
Usp18
IFIT3
ISG15
OAS1
PLSCR1
HERC6
CCL5
BIRC3
MMP1
SAMD9
IFNb1
NS
B
low
high
B16F0
Fold Change
STAT1
OASL
IFIT3
CCL5
C
H1299
low
high
cGAS
β-Actin
STAT1
β-Actin
60
40
80
40
D
unsorted
CD44+/CD24-
Fold Change
IFNB1
ISG15
IFIT2
IFIT3
E
unsorted
CD133+
Fold Change
IFNB1

Figure 2

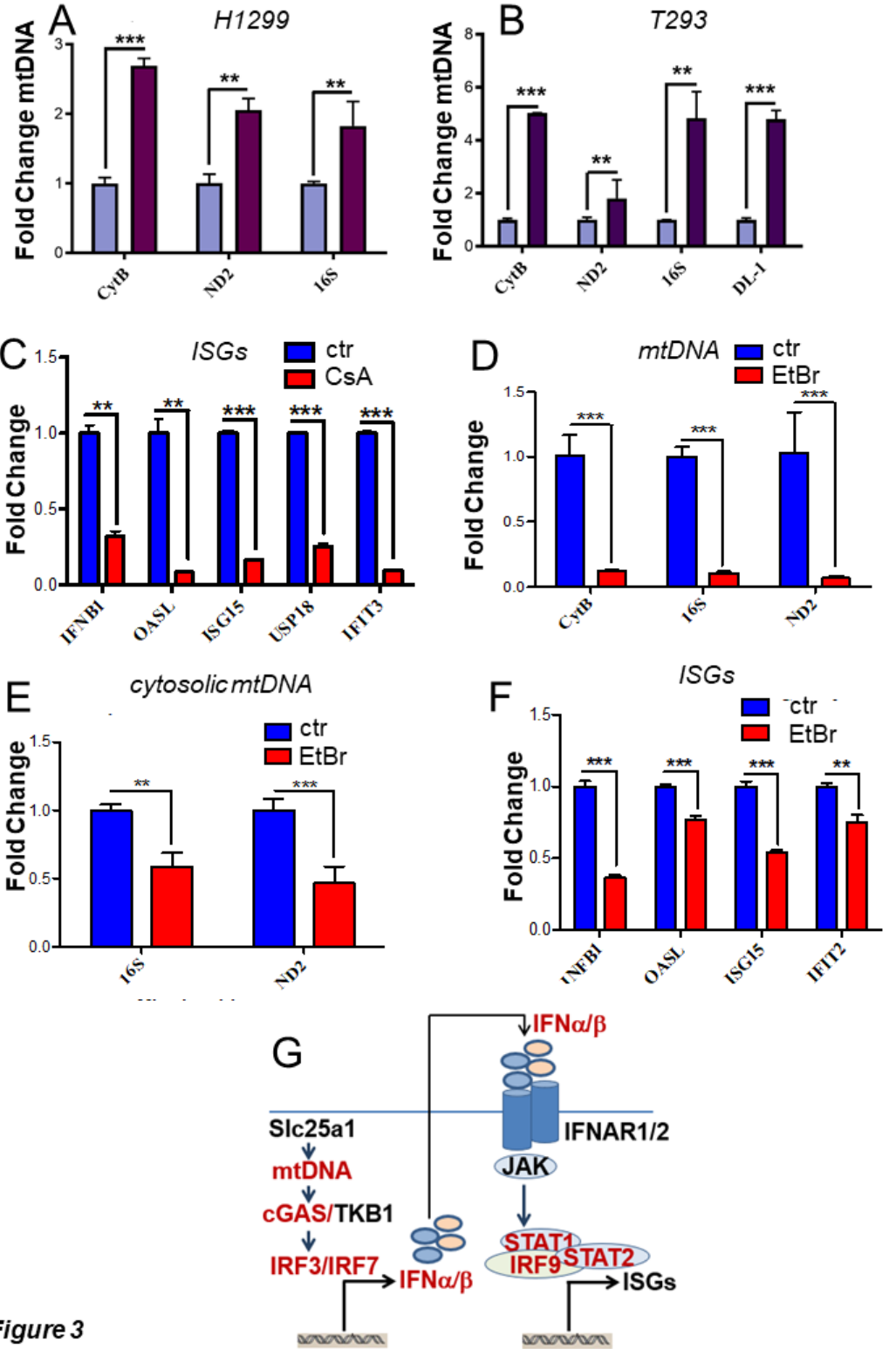
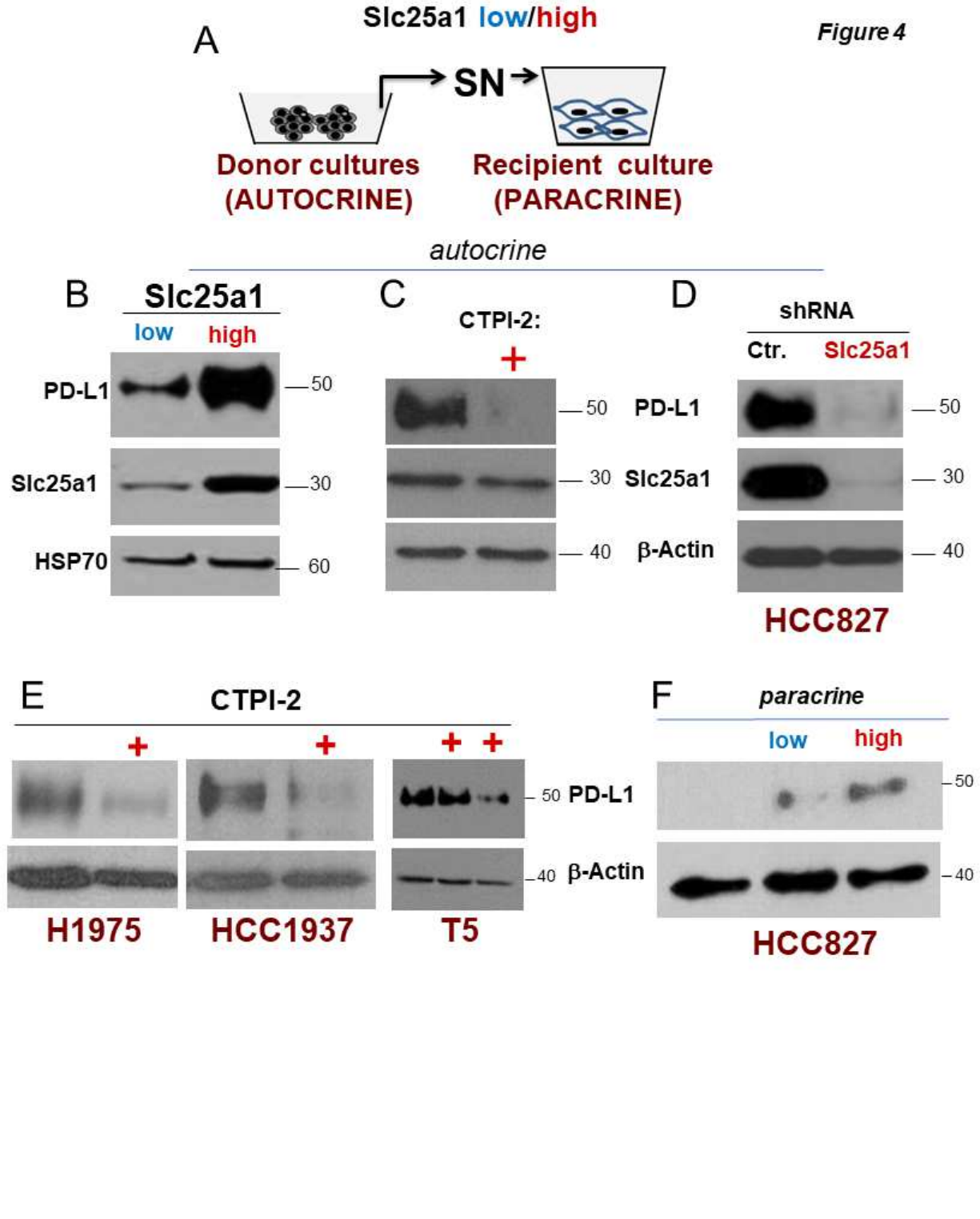

A
H1299
Fold Change mtDNA
CytB
ND2
16S
B
T293
DL-1
C
ISGs
ctr
CsA
Fold Change
IFNBI
OASL
ISG15
USP18
IFIT3
D
mtDNA
EtBr
E
cytosolic mtDNA
F
IFIT2
G
IFNα/β
Slc25a1
mtDNA
cGAS/TKB1
IRF3/IRF7
IFNAR1/2
JAK
STAT1
IRF9
STAT2
ISGs

Figure 3

Figure 4


A
Slc25a1 low/high
SN
Donor cultures
(AUTOCRINE)
Recipient culture
(PARACRINE)
autocrine
B
Slc25a1
low
high
PD-L1
Slc25a1
HSP70
50
30
60
C
CTPI-2:
+
50
30
40
D
shRNA
Ctr.
Slc25a1
PD-L1
Slc25a1
β-Actin
50
30
40
HCC827
E
CTPI-2
+
+
+ +
50
PD-L1
40
β-Actin
H1975
HCC1937
T5
F
paracrine
low
high
50
40
HCC827

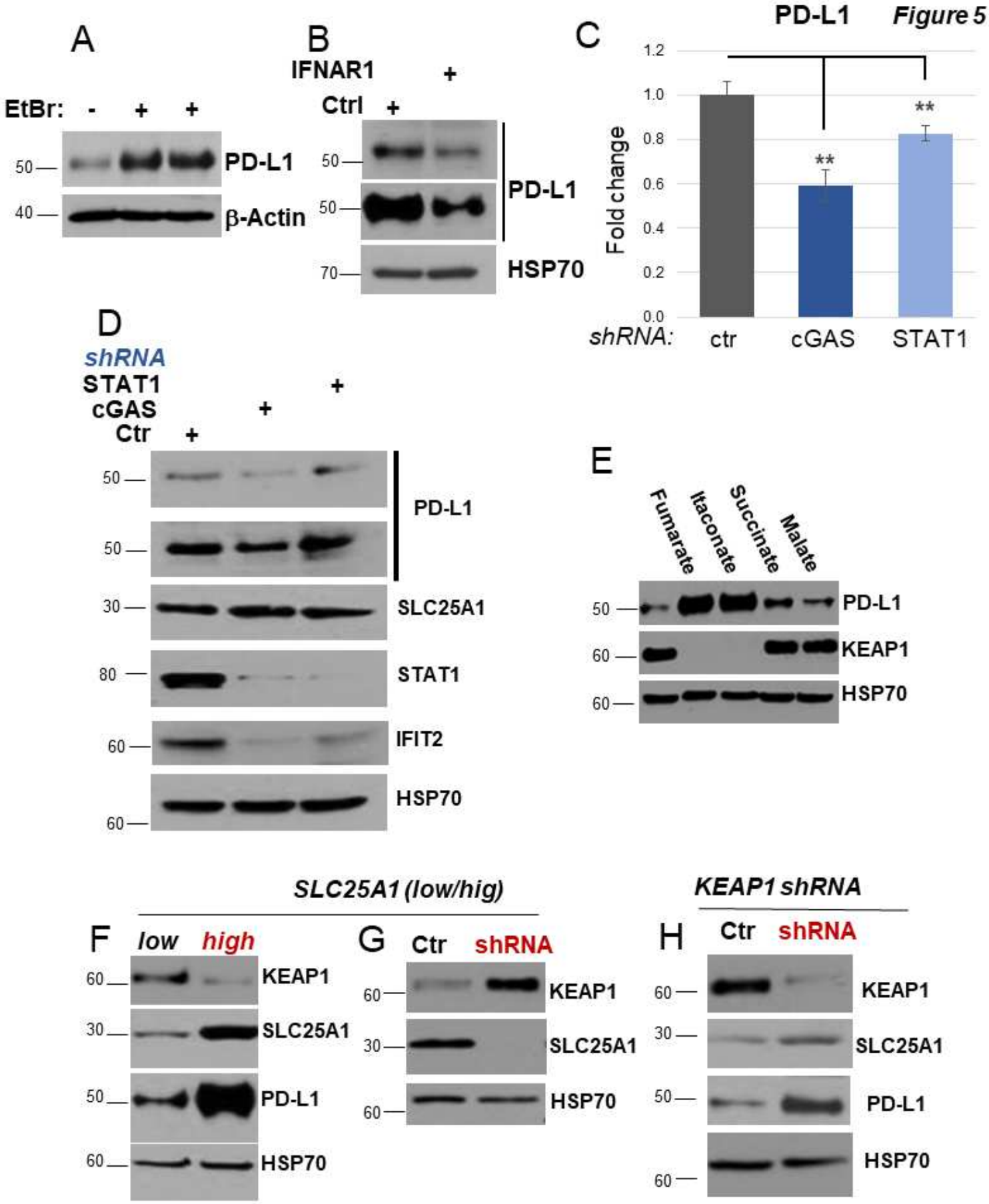
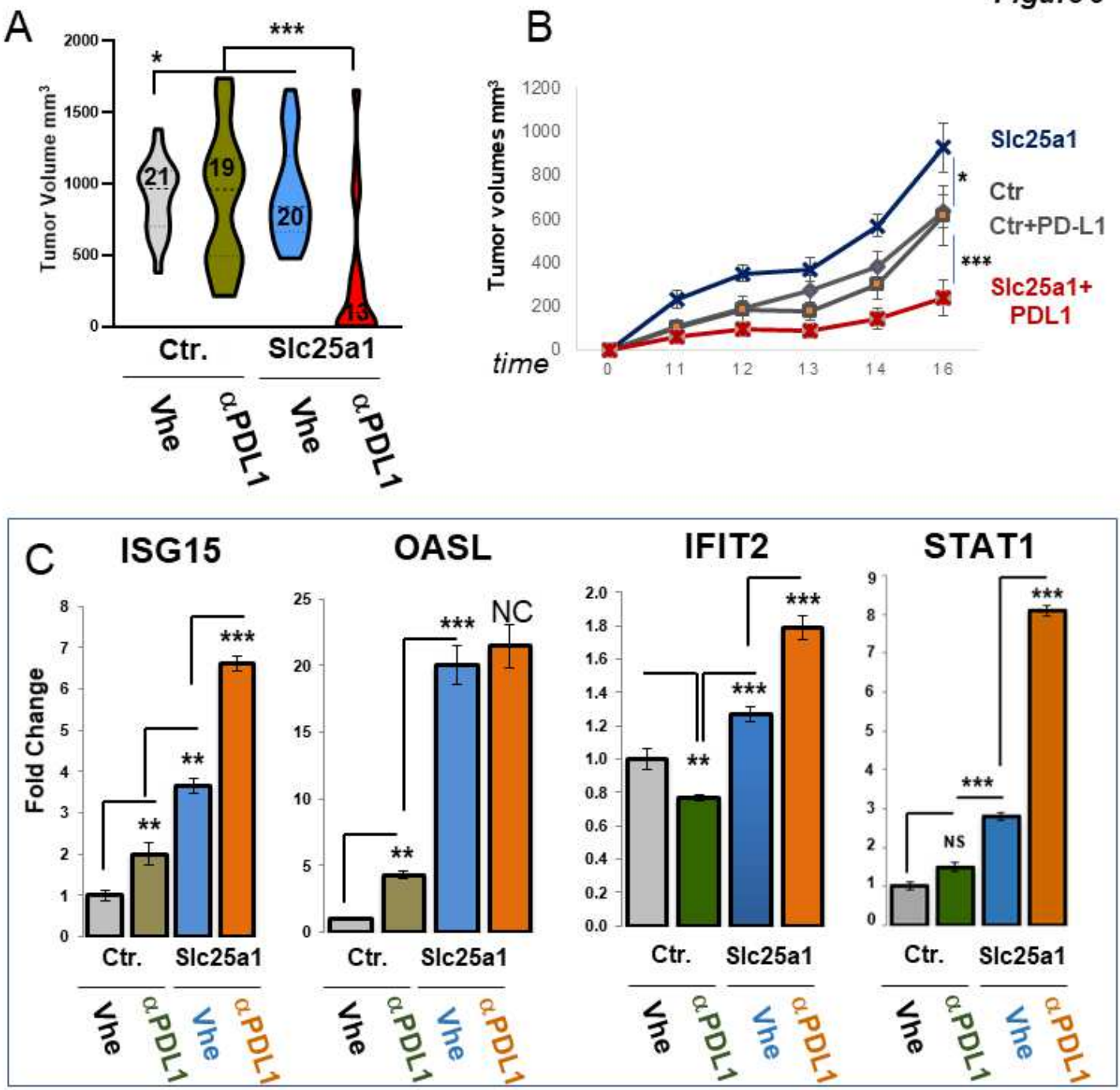

A
EtBr: - + +
50
PD-L1
40
β-Actin
B
IFNAR1 +
Ctrl +
50
PD-L1
50
70
HSP70
C
PD-L1
Figure 5
Fold change
1.2
1.0
0.8
0.6
0.4
0.2
0.0
**
**
shRNA:
ctr
cGAS
STAT1
D
shRNA
STAT1 +
cGAS +
Ctr +
50
PD-L1
50
30
SLC25A1
80
STAT1
60
IFIT2
60
HSP70
E
Fumarate
Itaconate
Succinate
Malate
50
PD-L1
60
KEAP1
60
HSP70
SLC25A1 (low/hig)
F
low
high
60
KEAP1
30
SLC25A1
50
PD-L1
60
HSP70
G
Ctr
shRNA
60
KEAP1
30
SLC25A1
60
HSP70
KEAP1 shRNA
H
Ctr
shRNA
60
KEAP1
30
SLC25A1
50
PD-L1
60
HSP70

Figure 6


A
Tumor Volume mm3
2000
1500
1000
500
0
*
***
21
19
20
13
Ctr.
Slc25a1
Vhe
αPDL1
Vhe
αPDL1
B
Tumor volumes mm3
1200
1000
800
600
400
200
0
time
0
11
12
13
14
16
Slc25a1
Ctr
Ctr+PD-L1
Slc25a1+ PDL1
*
***
C
ISG15
OASL
IFIT2
STAT1
Fold Change
NC
NS
**
***
Ctr.
Slc25a1
Vhe
αPDL1
Vhe
αPDL1

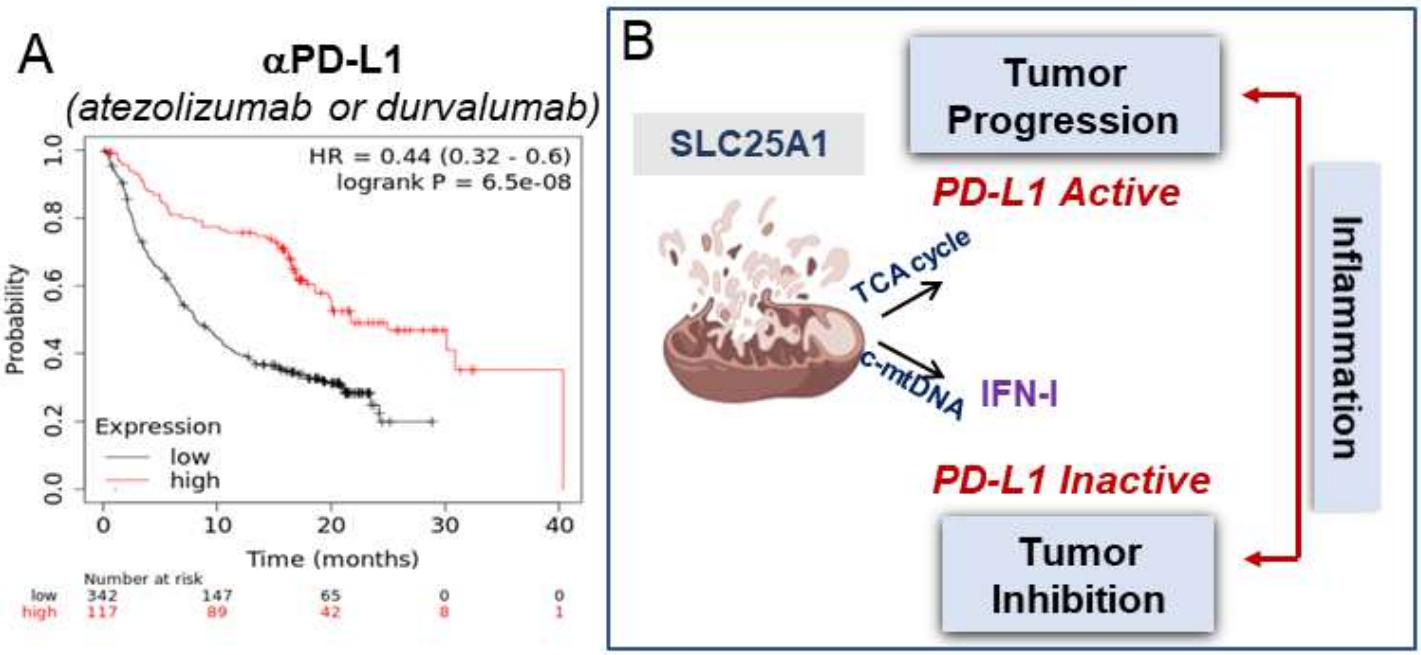

A
αPD-L1
(atezolizumab or durvalumab)
HR = 0.44 (0.32 - 0.6)
logrank P = 6.5e-08
Probability
0.0
0.2
0.4
0.6
0.8
1.0
Expression
low
high
0
10
20
30
40
Time (months)
Number at risk
low 342 147 65 0 0
high 117 89 42 8 1
B
SLC25A1
Tumor Progression
PD-L1 Active
TCA cycle
c-mtDNA
IFN-I
PD-L1 Inactive
Tumor Inhibition
Inflammation

Figure 7

Supplementary Files

This is a list of supplementary files associated with this preprint. Click to download.

- SupplementaryfileRM.pdf